Simulation and Modeling of Flow Generated by Gust Generator in a Wind Tunnel

Nhan Nguyen*
NASA Ames Research Center, Moffett Field, CA 94035
Juntao Xiong†
Stinger Ghaffarian Technologies, Inc., Moffett Field, CA 94035
Nicholas B. Cramer‡
NASA Ames Research Center, Moffett Field, CA 94035

A computational study of a gust field generated by a gust generator in a low-speed wind tunnel. The gust generator is designed for the University of Washington Aeronautical Laboratory (UWAL) Kirsten wind tunnel for a gust load alleviation (GLA) control experiment of a Common Research Model (CRM) flexible wing utilizing the Variable Camber Continuous Trailing Edge Flap (VCCTEF). The gust generator comprises four horizontal NACA 0015 gust generator vanes placed upstream of the test section. Computational fluid dynamics simulations using a two-dimensional (2D) Unsteady-Reynolds-Averaged-Navier-Stokes (URANS) with $k-\omega$ Shear Stress Transport (SST) turbulence model provide detailed time-resolved information about the generated flow by the gust generator under prescribed sinusoidal motion. The characteristics of the induced flow by the gust generator are analyzed. A gust propagation model of the gust field is investigated. An unsteady lift model is developed using a varying-fidelity approach which includes a 2D interference aerodynamic model of the combined gust generator-wing system. The computed integrated unsteady lift is compared to experimental data for validation of the unsteady lift model. Both the amplitude and transport delay are found to be accurately captured by the unsteady lift model.

I. Introduction

The aircraft industry has been responding to the need for energy-efficient aircraft by redesigning airframes to be aerodynamically efficient, employing light-weight materials for aircraft structures and incorporating more energy-efficient aircraft engines. Reducing airframe operational empty weight (OEW) using advanced composite materials is one of the major considerations for improving energy efficiency. Modern light-weight materials can provide less structural rigidity while maintaining sufficient load-carrying capacity. As structural flexibility increases, aeroelastic interactions with aerodynamic forces and moments can alter aircraft aerodynamics significantly.[1] One option for managing the aeroelastic behavior of the aircraft is through control system design. The control system could be made to both suppress undesirable motion and shape the flexible structure in pursuit of improved performance goals.

Gust disturbances are among the most critical load cases an aircraft can experience during service life. The increasing structural flexibility of modern commercial aircraft generally results in an increased sensitivity of the aircraft to gust loads which can affect structural integrity and ride quality. Researchers have been looking for solutions to reduce structural stresses at the wing root caused by gust encounters, either by using passive (e.g., aeroelastic composite tailoring) or active methods (e.g., deploying control surfaces). Some studies show that active aeroelastic wing shaping control can have a potential gust load alleviation (GLA)

*Senior Research Scientist and Technical Group Lead, Associate Fellow AIAA, Intelligent Systems Division, nhan.t.nguyen@nasa.gov
†Aerospace Engineer, Intelligent System Division, Nicholas.b.cramer@nasa.gov
‡Aerospace Engineer, Intelligent System Division, Nicholas.b.cramer@nasa.gov

benefit. A new flap concept, referred to as the Variable Camber Continuous Trailing Edge Flap (VCCTEF) system, was conceived by NASA.[2–4]

A wind tunnel experiment is currently being planned at University of Washington (UW) to demonstrate active GLA control on a flexible wing with the VCCTEF. Figure 1 shows a sub-scale wind tunnel model of the Common Research Model (CRM) wing with active VCCTEF. For some applications, the VCCTEF system offers potential pay-off in drag reduction and GLA by actively controlling the shape of the wing.[5] The experimental validation of this active control technology on a scaled aeroelastic model is challenging in terms of the aeroservoelastic (ASE) models which consider the gust propagation decay and transport lag effects.

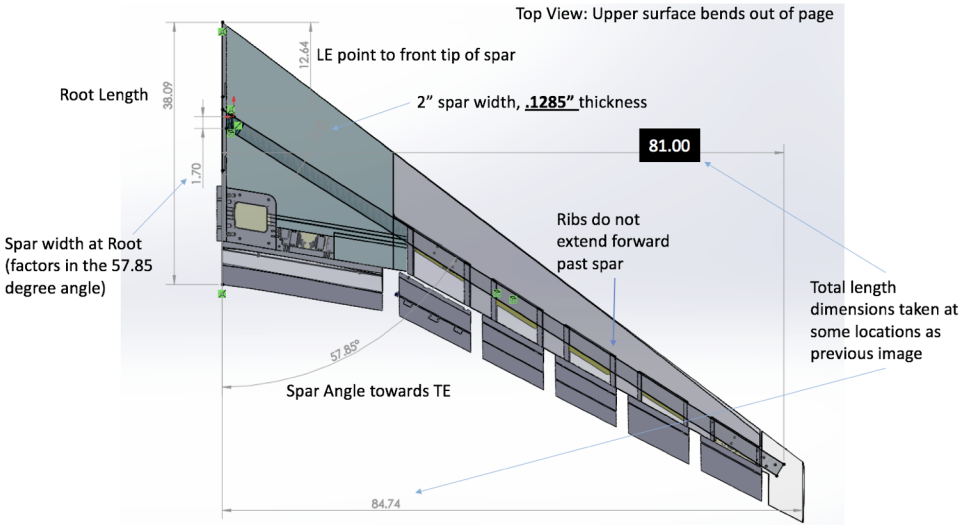

Figure 1. CRM Wing Wind Tunnel Model with Active VCCTEF

The experimental set up includes a new gust generator system installed in the test section of the Kirsten wind tunnel (KWT) at UW, as shown in Fig. 2. The gust generator comprises four vanes installed upstream of the test section. The vanes are driven by a drive motor to provide the gust excitation to the CRM wing. A flow characterization test has been performed to characterize the flow downstream from the vanes using a pressure rake, as shown in Fig. 2.

Figure 2. Gust Generator in Kirsten Wind Tunnel at University of Washington

Experimental and computational studies of gust generators have been made by many other research groups.[6–12, 12, 13, 13, 14, 14–25] They either use a single vane or multi-vane system with symmetric NACA airfoils ahead of the test model to disturb the flow for the disturbance generation. To better understand the phenomena of the gust generation and propagation for the purpose of estimating the unsteady lift generated by the gust generator to be used in the ASE model, a computational study is performed in this paper. An open-source Computational Fluid Dynamics (CFD) software, OpenFOAM,[27] is used for this study. Computations using two-dimensional (2D) Unsteady-Reynolds-Averaged-Navier-Stokes (URANS) with the $k-\omega$ SST turbulence model provide detailed time-resolved information about the induced flow by the gust generator in the vertical plane. The characteristics of the induced flow by the gust generator are analyzed in section III. A gust propagation model of the gust field is investigated in section IV and used to develop an unsteady gust model in section IV.

II. Computational Approach

A. Governing Equation

The incompressible URANS equations are expressed as follows:

$$\sum_{i=1}^{3} \frac{\partial u_i}{\partial x_i} = 0 \tag{1}$$

$$\rho\left(\frac{\partial u_i}{\partial t} + \frac{\partial u_i u_j}{\partial x_j}\right) = -\frac{\partial p}{\partial x_i} + \frac{\partial \tau_{ij}}{\partial x_j} \tag{2}$$

where the viscous shear stress tensor τ_{ij} is given by

$$\tau_{ij} = \tau_{ij}^{L} + \tau_{ij}^{T} \tag{3}$$

$$\tau_{ij}^{L} = \mu\left(\frac{\partial u_i}{\partial x_j} + \frac{\partial u_j}{\partial x_i}\right) - \frac{2}{3}\mu\frac{\partial u_k}{\partial x_k}\delta_{ij} \tag{4}$$

The closure turbulence model used to evaluate the turbulent shear stress τ_{ij}^{T} and viscosity μ is the $k-\omega$ SST turbulence model.[28] The SST turbulence model combines the advantages of the $k-\omega$ and $k-\epsilon$

turbulence models to give superior performance in simulating the wall boundary layer and free stream flow, thus the $k-\omega$ SST model is chosen for all the cases in this study. The equations are

$$\frac{\partial k}{\partial t}+u_j\frac{\partial k}{\partial x_j}=P-\beta^*\omega k+\frac{\partial}{\partial x_j}\left[\left(\nu+\sigma_k\nu_T\right)\frac{\partial k}{\partial x_j}\right] \tag{5}$$

$$\frac{\partial \omega}{\partial t}+u_j\frac{\partial \omega}{\partial x_j}=\frac{\gamma}{\nu_T}P-\beta\omega^2+\frac{\partial}{\partial x_j}\left[\left(\nu+\sigma_\omega\nu_T\right)\frac{\partial \omega}{\partial x_j}\right]+2\left(1-F_1\right)\frac{\sigma_{\omega 2}}{\omega}\frac{\partial k}{\partial x_j}\frac{\partial \omega}{\partial x_j} \tag{6}$$

where

$$P=\frac{\tau_{ij}}{\rho}\frac{\partial u_i}{\partial x_j} \tag{7}$$

The turbulent eddy viscosity is given by

$$\nu_T=\frac{a_1 k}{\max\left(a_1\omega,\Omega F_2\right)} \tag{8}$$

$$\mu_T=\rho\nu_T \tag{9}$$

The turbulent shear stress is calculated using

$$\tau_{ij}^T=2\mu_T\left(S_{ij}-\frac{1}{3}\frac{\partial u_k}{\partial x_k}\right)-\frac{2}{3}\rho k\delta_{ij} \tag{10}$$

F_1 and F_2 represent blending functions. The model constants can be calculated by

$$\phi=F_1\phi_1+\left(1-F_1\right)\phi_1 \tag{11}$$

B. Numerical Solver

In this study, the open source CFD solver OpenFOAM is used to solve the governing equations. The PIMPLE solver, with dynamic mesh moving package added, is used for the unsteady incompressible flow simulation.[28] The finite-difference schemes used are second-order accurate in both space and time. The time discretization is second-order implicit backward differencing. Gaussian integration is used for the spatial discretization, with linear interpolation from cell centers to cell faces for second-order derivatives.

C. Computational Model and Mesh

The University of Washington Aeronautical Laboratory (UWAL) KWT is a subsonic, closed-circuit, double-return wind tunnel. The wind tunnel has a test section with a rectangular 8 ft x 12 ft cross section that is 10 feet long. Due to the cross-section size limitation and the requirement of the generated gust magnitude, a four-vane gust generator configuration is suitable for this wind tunnel. The new gust generator is designed and fabricated specifically for this active GLA control experiment. The gust generator comprises four vanes installed upstream of the test section. The vanes are driven by a drive motor to provide the gust excitation to the CRM wing. The vanes have a 15-inch chord. The center of rotation of the vanes is at 30% chord. The cross section of the vanes is a NACA 0015 airfoil with a modified trailing edge portion having a straight line connecting the maximum thickness location to the trailing edge location. The vanes are spaced 17 inches apart vertically. The top and bottom vanes are at a distance of 22.5 inches from the ceiling and floor of the test section. The trailing edge plane of the vanes is physically verified to be 14.64 inches ahead of the leading edge of the wing root section. Thus, the wing and the vanes are an aerodynamically coupled system. Figure 3 shows the dimensions of the gust generator vanes in relation to the wing airfoil sections. In order to investigate the induced gust field and unsteady aerodynamic loading on the downstream CRM wing, four different configurations are simulated, which are shown in Fig. 4. Figure 5 shows the computational mesh around the vanes. The grid is clustered near the vane walls to resolve the boundary layer.

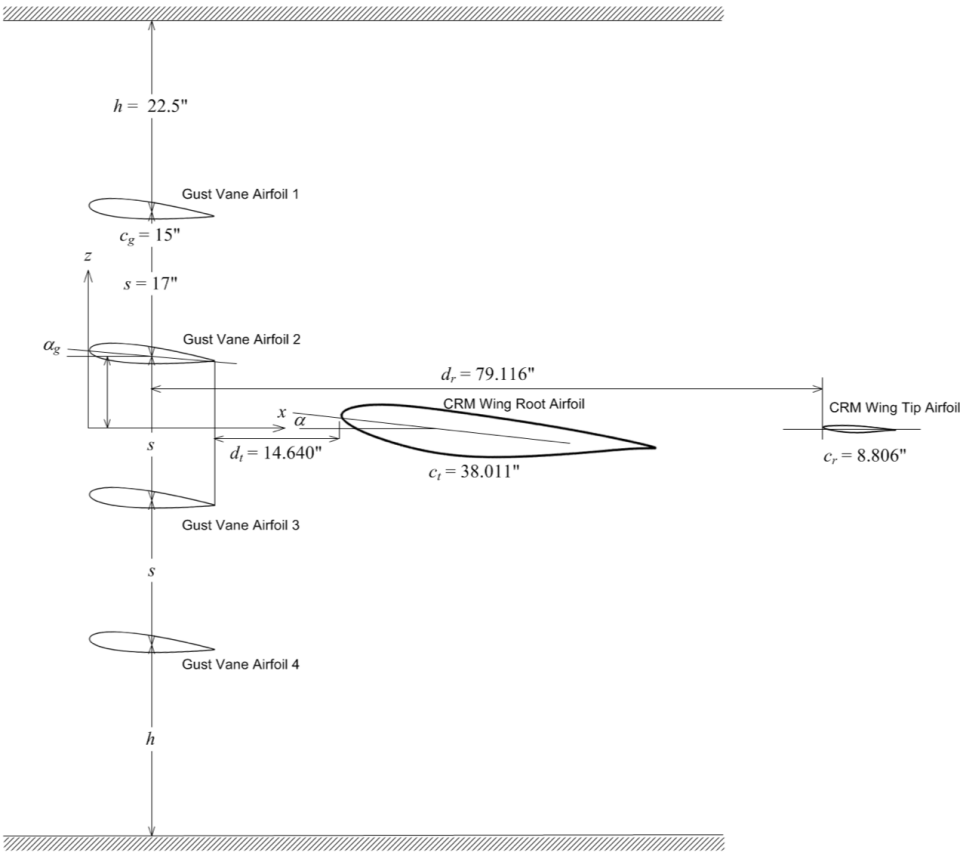

Figure 3. Gust Vane Dimensions in Relation to CRM Wing Airfoil Sections.

(a) Vane Only

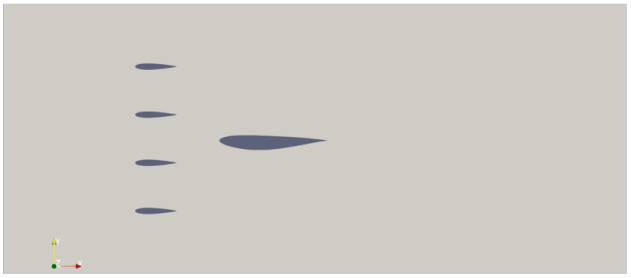

(b) Vane and CRM Wing Root Airfoil

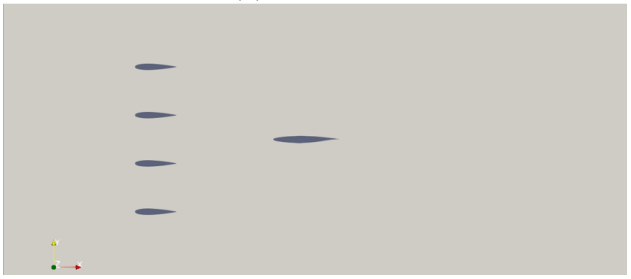

(c) Vane and CRM Wing Yehudi Airfoil

(d) Vane and CRM Wing Tip aAirfoil

Figure 4. Computational Configurations

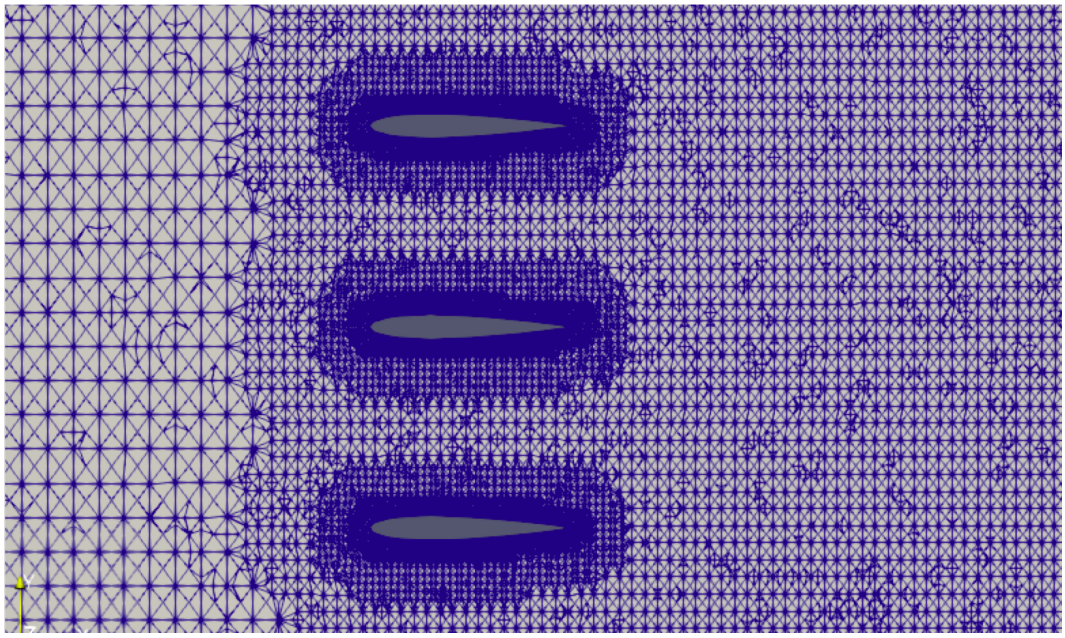

Figure 5. Computational Mesh

D. Boundary Conditions

The streamwise velocity is specified at the inlet surface. In this study, the inlet flow velocity is 25 m/s or 82 ft/s. This corresponds to a dynamic pressure of 8 psf. The test dynamic pressure is at a nominal 10 psf value. At the outlet surface, the static pressure is specified. An adiabatic no-slip boundary conditions are specified on the top and bottom wind tunnel walls as well as the vane surfaces.

III. Computational Results

A grid independence study is first performed. Then, the gust generator-induced flow is simulated with different gust generator vane motion amplitudes and frequencies. Thirdly, the induced aerodynamic loading on the CRM wing airfoils at the root, Yehudi break, and tip stations are then simulated. A gust propagation model of the gust field is studied. Finally, an unsteady lift model is developed to estimate the unsteady lift on the CRM wing. The results are then compared to wind tunnel data to validate the model.

A. Grid Independence Study

Three meshes with different sizes: coarse, medium, and fine, with a total of 8.0×10^4, 13.2×10^4, and 27.5×10^4 nodes, respectively, are used for the grid independence study. Figure 6 shows a comparison between grid levels of the induced vertical velocity along the centerline at 2 ft downstream of the trailing edge of the vane. The prescribed gust generator vane motion is sinusoidal with a frequency of 2 Hz and an amplitude of 10°. The velocity profiles are almost identical for the medium and fine mesh levels. This confirms that grid independence has been achieved. To reduce computational costs, the remaining simulations are performed with the medium size mesh.

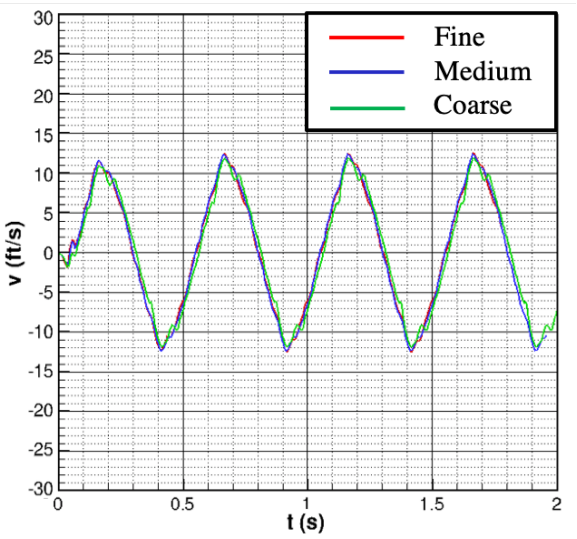

Figure 6. Grid Independence Study

B. Characteristics of The Induced Flow

In this section, the gust generator induced flow is simulated with different amplitudes and frequencies applied to the gust generator vane motion. Figures 9-8 show the vertical velocity contours for one period, denoted by T, during the prescribed sinusoidal motion of the gust generator vanes. Two amplitudes of 5° and 10° and two frequencies of 1 Hz and 2 Hz are used. The vertical velocity is induced by the gust generator to generate an induced wave that propagates downstream. Due to the viscous dissipation of the air and top-bottom wall boundaries, the magnitude of the vertical velocity decreases as the induced wave moves downstream, especially for the low 1 Hz frequency case. Figures 13-12 show the vertical velocity profiles at three downstream locations from the vane trailing edge along the center line with different amplitudes and frequencies applied to the gust generator vane motion. The 10° vane sinusoidal motion amplitude of the vane sinusoidal motion could generate a larger vertical velocity downstream; however, there appears high frequency contents in the induced vertical velocity downstream for this case, particularly for the low frequency vane sinusoidal motion. This observation indicates that the 10° vane sinusoidal motion amplitude is probably too large and the gust generator vanes may be at a stall onset. Figures 13-12 also show that the induced vertical velocity decays as the induced wave moves downstream.

(a) $t = 0/4T$

(b) $t = 1/4T$

(c) $t = 2/4T$

(d) $t = 3/4T$

Figure 7. Vertical Velocity Contours for One Period ($5^\circ \sin 2\pi ft$, $f = 1$ Hz)

(a) $t = 0/4T$

(b) $t = 1/4T$

(c) $t = 2/4T$

(d) $t = 3/4T$

Figure 8. Vertical Velocity Contours for One Period ($5^\circ \sin 2\pi ft$, $f = 2$ **Hz**)

(a) $t = 0/4T$

(b) $t = 1/4T$

(c) $t = 2/4T$

(d) $t = 3/4T$

Figure 9. Vertical Velocity Contours for One Period ($10^\circ \sin 2\pi ft$, $f = 1$ **Hz**)

(a) $t = 0/4T$

(b) $t = 1/4T$

(c) $t = 2/4T$

(d) $t = 3/4T$

Figure 10. Vertical Velocity Contours for One Period ($10^\circ \sin 2\pi f t$, $f = 2$ **Hz**)

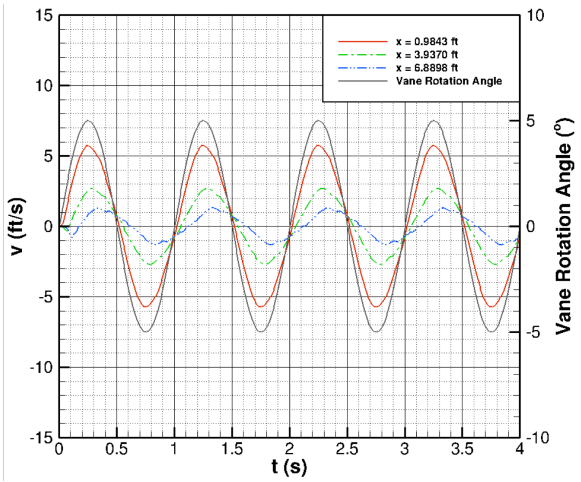

Figure 11. Comparison of Induced Velocity at the Center Line ($5^\circ \sin 2\pi ft$, $f = 1$ **Hz**)

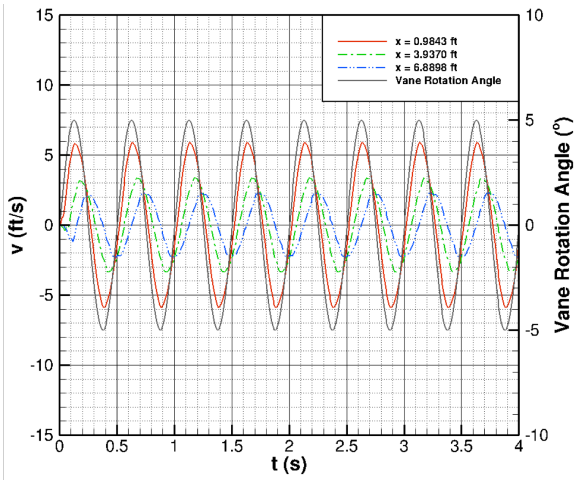

Figure 12. Comparison of Induced Velocity at the Center Line ($5^\circ \sin 2\pi ft$, $f = 2$ **Hz**)

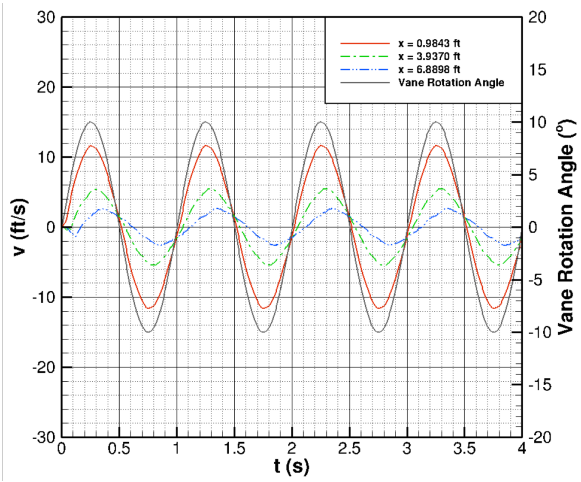

Figure 13. Comparison of Induced Velocity at the Center Line ($10^\circ \sin 2\pi ft$, $f = 1$ **Hz**)

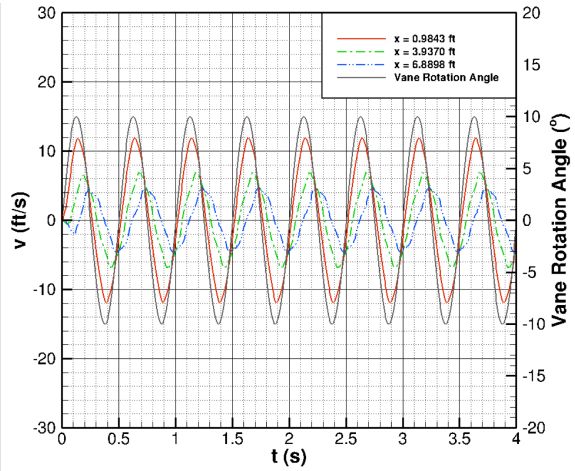

Figure 14. Comparison of Induced Velocity at the Center Line ($10^\circ \sin 2\pi ft$, $f = 2$ **Hz**)

C. Induced Aerodynamic Loading

In order to explore the response of an airfoil subjected to a gust load, the CRM airfoils at the root, Yehudi break, and tip stations are placed downstream of the gust generator. Based on the simulation results shown in Section III.B and the GLA test requirement, an amplitude of 5° and a frequency 2 Hz is used in the simulation to investigate the induced unsteady aerodynamic loading on the CRM wing airfoils. Figures 15-17 show the vertical velocity contours for one period during the prescribed sinusoidal gust generator vane motion. For the vane motion with an amplitude of 5°, the flow is smooth and no flow separation is observed. However, a strong flow interaction is observed for the vane and CRM wing root airfoil case since the root airfoil is very close to the gust generator vane trailing edge. Figures 18 show the vertical velocity profiles at three locations between the gust generator vane trailing edge and the CRM wing airfoil leading edges along the center line. The decay of the induced vertical velocity and the transport lag response are observed. Figure 19 shows the induced unsteady lift coefficients on the CRM wing airfoils. Phase lags in the unsteady lift coefficients are also observed.

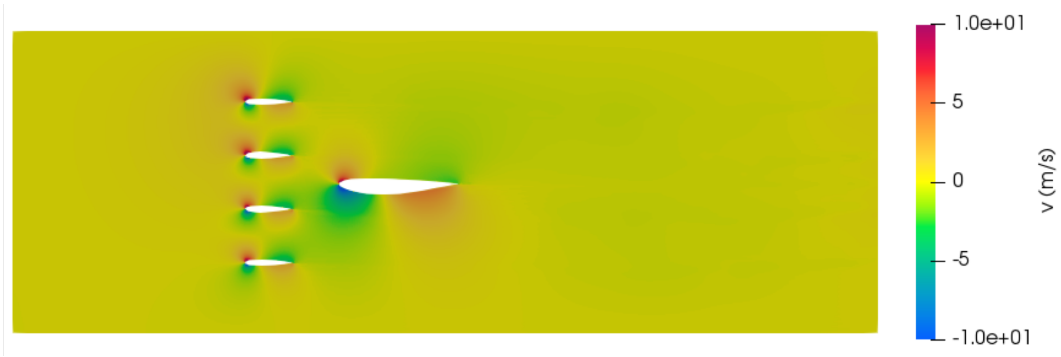

(a) $t = 0/4T$

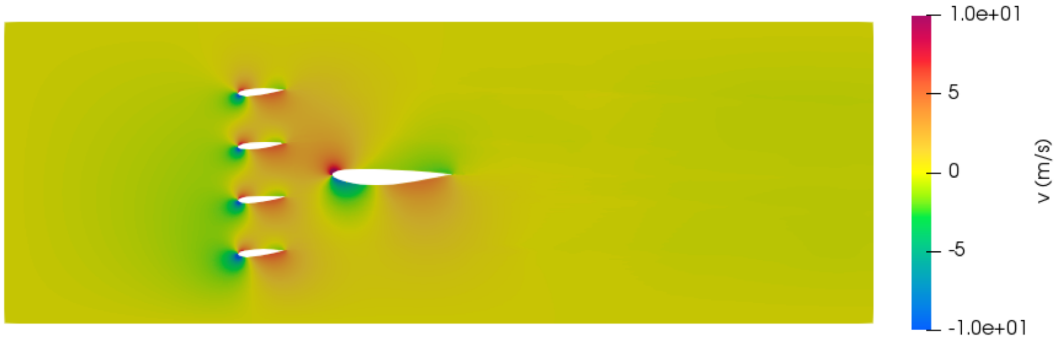

(b) $t = 1/4T$

(c) $t = 2/4T$

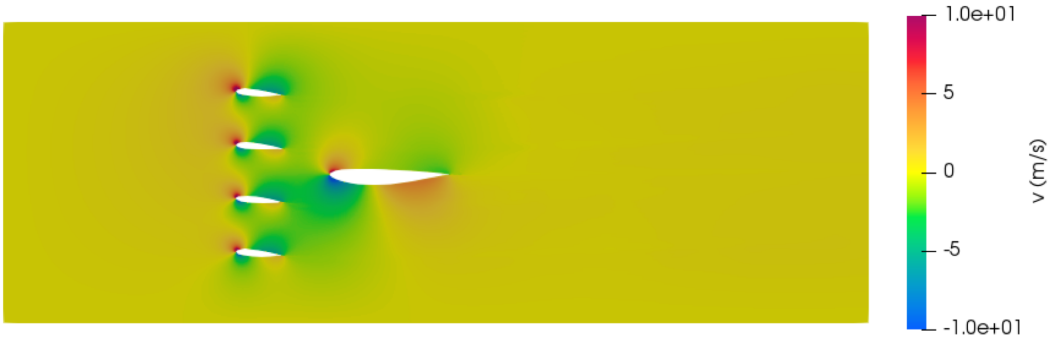

(d) $t = 3/4T$

Figure 15. Vertical Velocity Contours for One Period for Vane and Root Airfoil Configuration ($5^\circ \sin 2\pi ft$, $f = 2$ **Hz**)

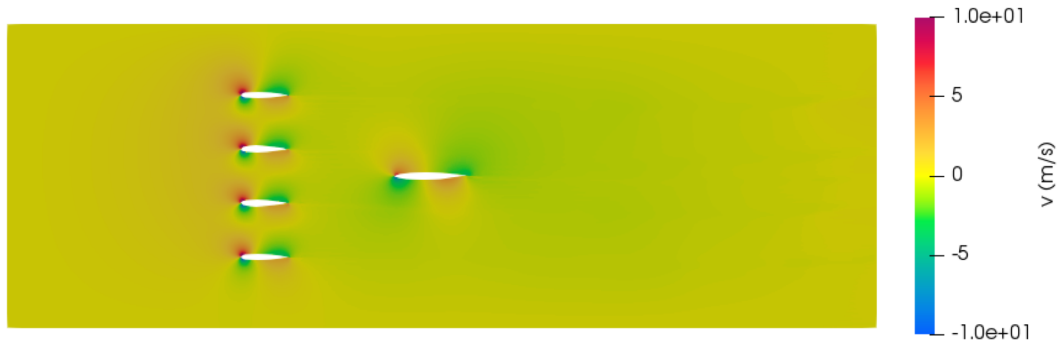

(a) $t = 0/4T$

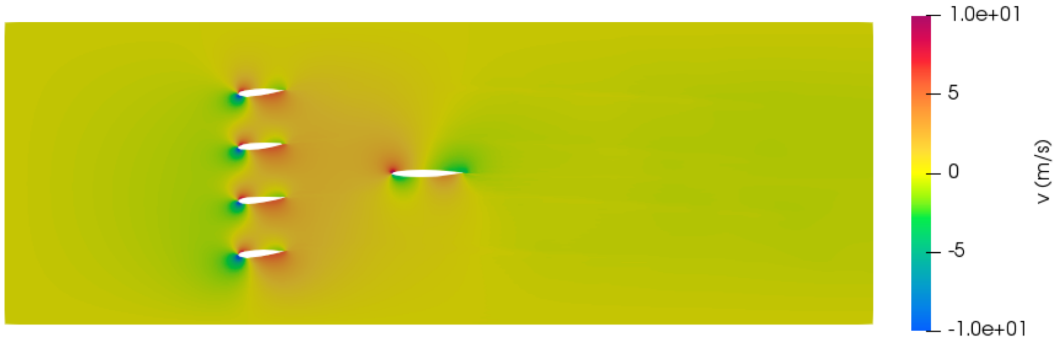

(b) $t = 1/4T$

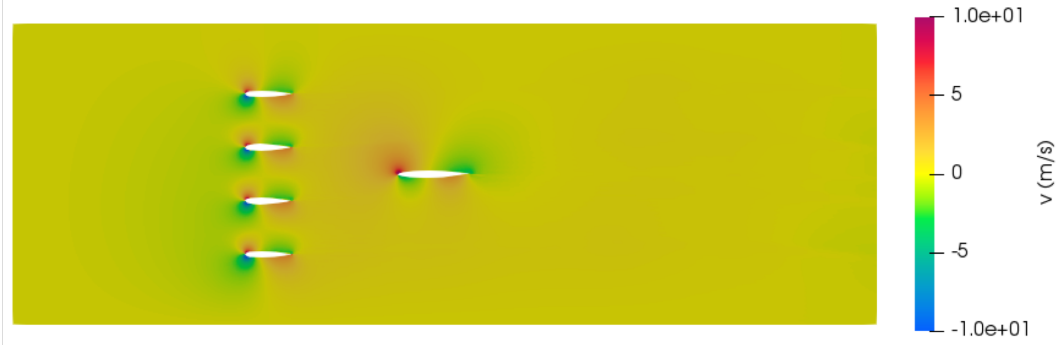

(c) $t = 2/4T$

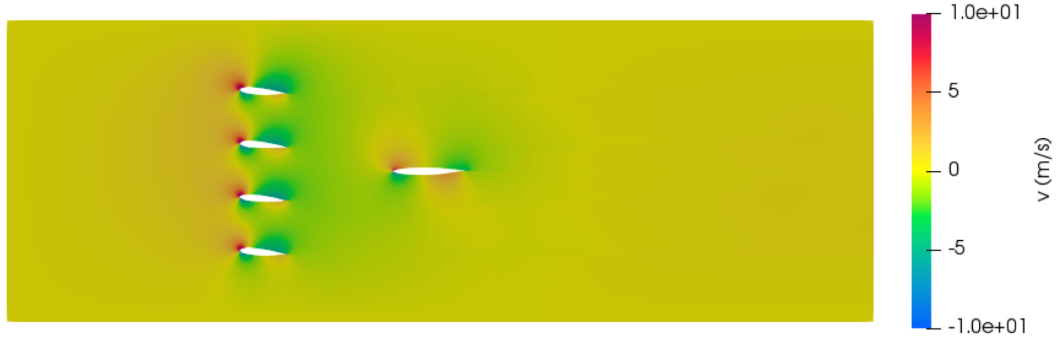

(d) $t = 3/4T$

Figure 16. Vertical Velocity Contours for One Period for Vane and Yehudi Airfoil Configuration ($5^\circ \sin 2\pi ft$, $f = 2$ **Hz)**

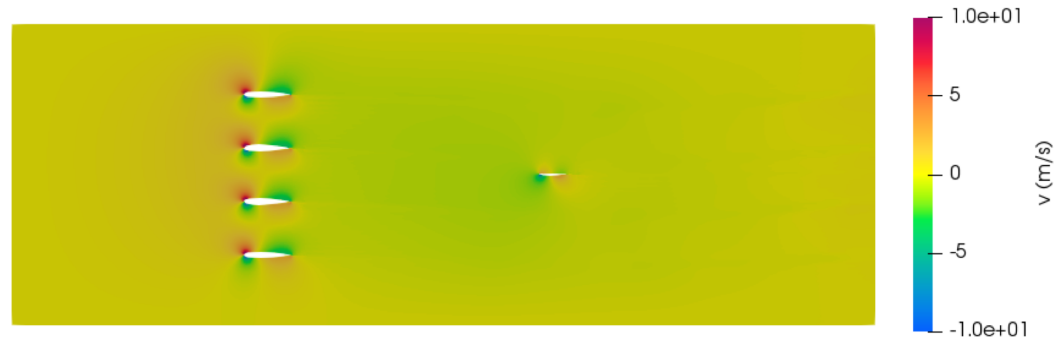

(a) $t = 0/4T$

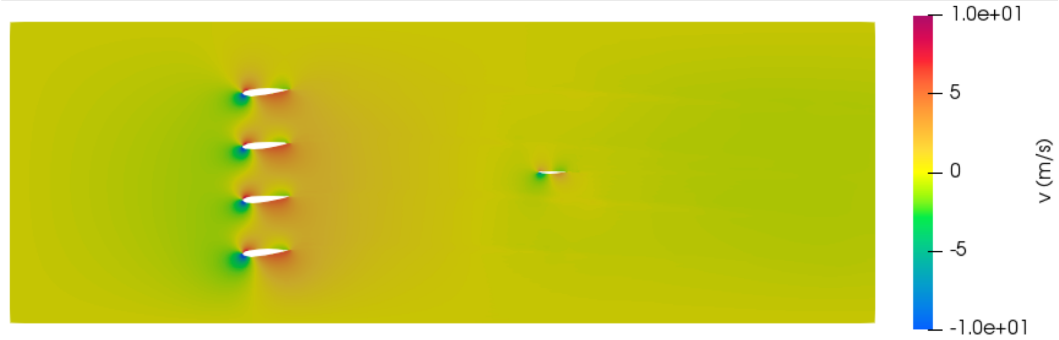

(b) $t = 1/4T$

(c) $t = 2/4T$

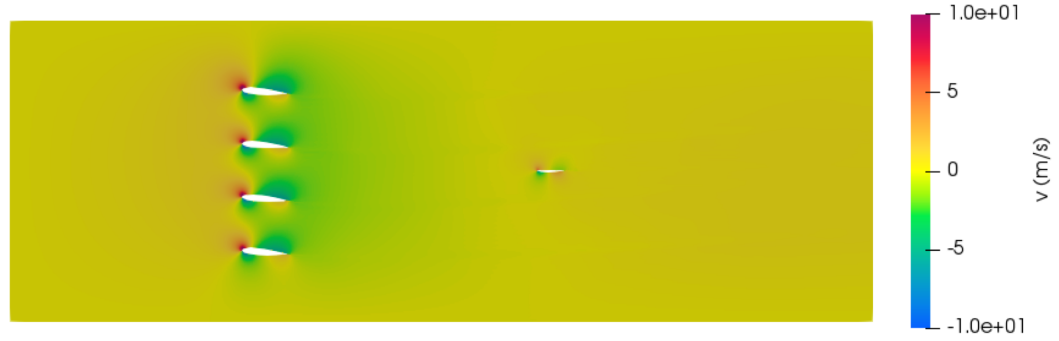

(d) $t = 3/4T$

Figure 17. Vertical Velocity Contours for One Period for Vane and Tip Airfoil Configuration ($5^\circ \sin 2\pi ft$, $f = 2$ Hz)

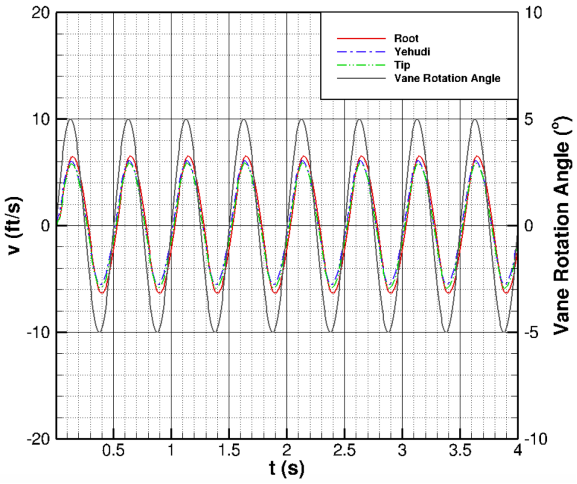

(a) Near Vane Trailing Edge

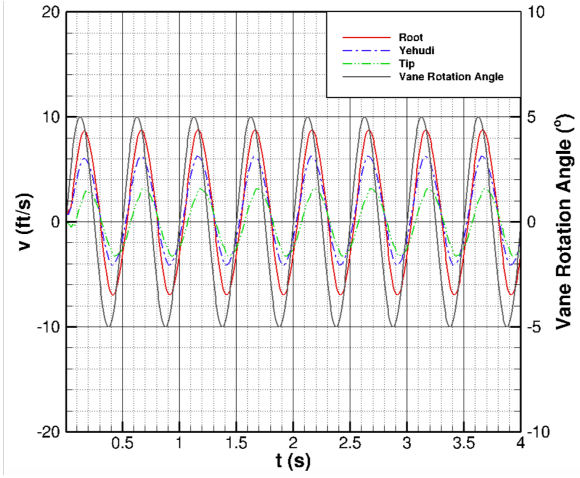

(b) Mid-Point between Vane Trailing Edge and CRM Wing Airfoil Leading Edge

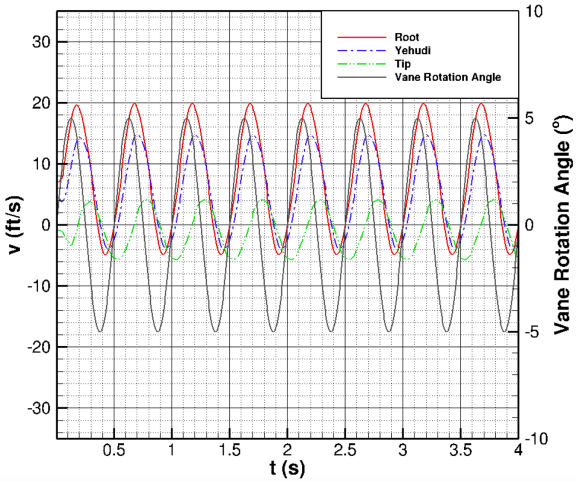

(c) Near CRM Airfoil Leading Edge

Figure 18. Comparison of Induced Velocity at the Center Line for Vane and CRM Wing Airfoils ($5° \sin 2\pi ft$, $f = 2$ **Hz)**

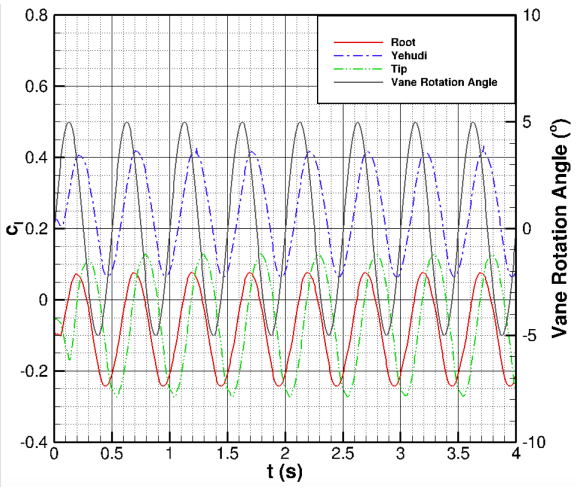

Figure 19. Unsteady Lift Coefficients of the CRM Wing Airfoils ($5^\circ \sin 2\pi f t$, $f = 2$ **Hz**)

IV. Gust Propagation Model

To estimate the unsteady lift on a wing section, the wake velocity field data from the simulations are used to determine the instantaneous gust angle of attack at the wing leading edge due to the gust generator vane motion. Because the wing airfoil creates a local upwash at the leading edge, it is difficult to determine the unperturbed gust angle of attack. Therefore, the wake velocity field data from the simulations of the gust generator vanes alone are used. Two quantities are extracted from the CFD simulation data, the aerodynamic lag and the amplitude of the gust angle of attack at the wing leading edge along the center of the wind tunnel and at other vertical positions.

The gust generator vane motion is prescribed by a pitch angle command

$$\theta_v(t) = -\theta_0 \sin \omega t \tag{12}$$

where the negative angle indicates a leading edge down pitch rotation. Assuming a small perturbation and the flow is not separated, the gust generator vane motion generates a gust field propagating downstream the gust generator vane trailing edge. This gust field can be characterized by a gust angle of attack described by

$$\alpha_g(x,z,t) = r(x,z)\,\theta_v(t - t_d(x,z)) = r(x,z)\,\theta_0 \sin\omega(t - t_d(x,z)) \tag{13}$$

where x is the axial position from the gust generator vane trailing edge, z is the vertical position with the positive sign convention denoting a position above the centerline, $r(x,z)$ is the ratio of the gust angle of attack to the gust vane amplitude and $t_d(x,z)$ is the gust aerodynamic lag. This can also be written as

$$\alpha_g(x,z,t) = -r(x,z)\,\theta_v(t)\cos\omega t_d t_d(x,z) + r(x,z)\,\frac{\dot{\theta}_v(t)}{\omega}\sin\omega t_d t_d(x,z) \tag{14}$$

We define the gust angle

$$\theta_g(x,z) \doteq r(x,z)\,\theta_0 = \bar{\theta}_g(x,z) + \Delta\theta_g(x,g) \tag{15}$$

where $\bar{\theta}_g(x,z)$ is the mean gust angle and $\Delta\theta_g(x,z)$ is the gust angle amplitude, and the dimensionless transport lag as

$$\tau_d(x,z) = \frac{2U_\infty t_d(x,z)}{c_v} \tag{16}$$

where c_v is the gust generator chord. Then, we express the gust angle of attack as

$$\alpha_g(x,z,t) = \theta_g(x,z)\sin k_v(\tau - \tau(x,z)) \tag{17}$$

where $\tau = \frac{2U_\infty t}{c_v}$ is a dimensionless time and $k_v = \frac{\omega c_v}{2U_\infty}$ is the reduced frequency of the gust generator vanes.

Figures 20-31 present the data on the gust angle amplitudes, mean gust angles, and transport delays of the gust fields created by the gust generator alone for the gust generator vane motion amplitudes of 5° and 10° and frequencies of 1 Hz and 2 Hz. The data of interest for use to develop the unsteady lift on the wing are those at $z = 0$. The mean gust angles are nearly zeros for all the cases. As the flow moves toward the test section floor and ceiling, the mean gust angles increase with the largest amplitude of 1° for the 5° amplitude 1 Hz frequency case. The gust angle amplitudes are seen to decrease rapidly and reach steady-state values after a distance of about $6c_v$. The dimensionless transport delays for all the cases seem to have consistent values of about 20 at a distance of $6c_v$. Note that the dimensionless transport delay due to a uniform flow is estimated to be $2\left(\frac{x}{c_v} + 0.25\right)$ using the assumption that the flow propagates from the three-quarter chord of the gust generator vanes. Thus, the transport delay in an oscillating flow field is greater than that in an uniform flow flow field.

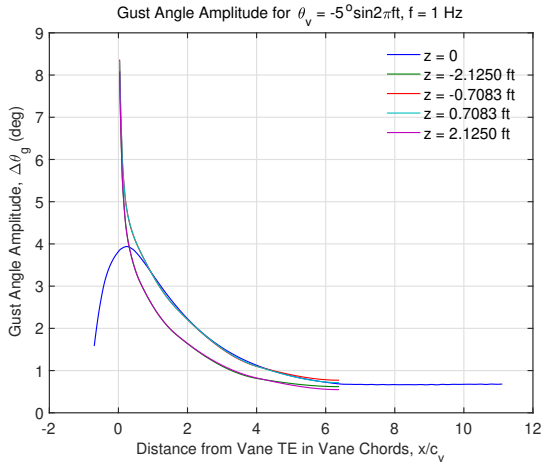

Figure 20. Gust Angle Amplitude for $5^\circ \sin 2\pi ft$**,** $f = 1$ **Hz,** $k_v = 0.0479$

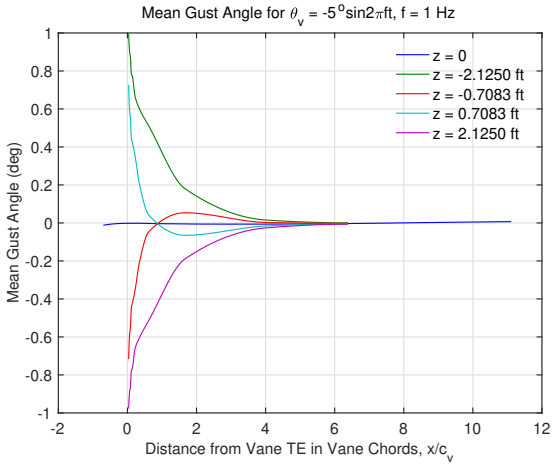

Figure 21. Mean Gust Angle for $5^\circ \sin 2\pi ft$**,** $f = 1$ **Hz,** $k_v = 0.0479$

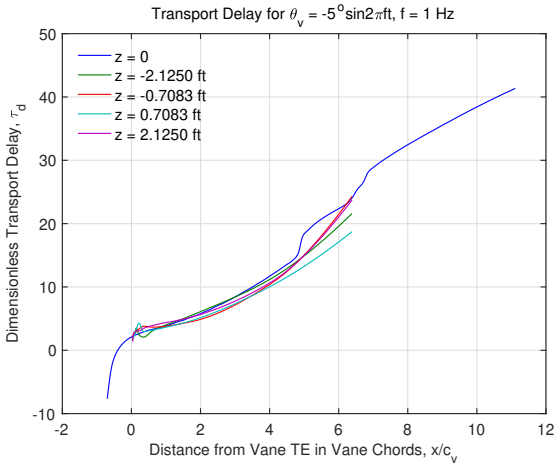

Figure 22. Gust Transport Delay for $5^\circ \sin 2\pi ft$, $f = 1$ Hz, $k_v = 0.0479$

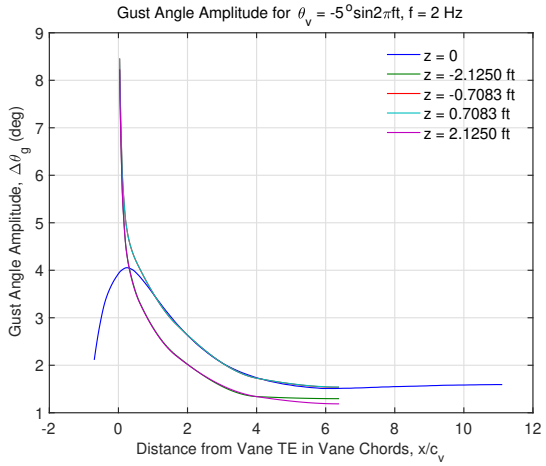

Figure 23. Gust Angle Amplitude for $5^\circ \sin 2\pi ft$, $f = 2$ Hz, $k_v = 0.0958$

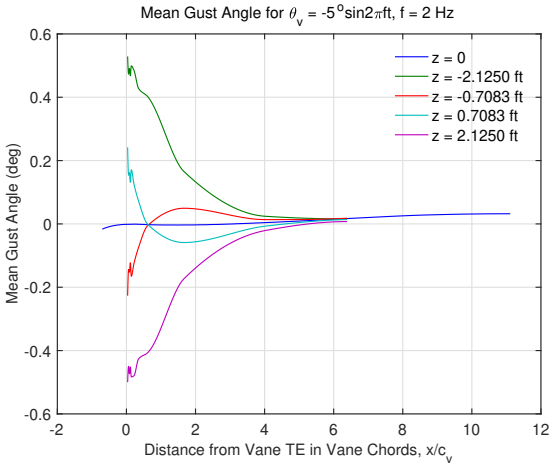

Figure 24. Mean Gust Angle for $5^\circ \sin 2\pi ft$, $f = 2$ Hz, $k_v = 0.0958$

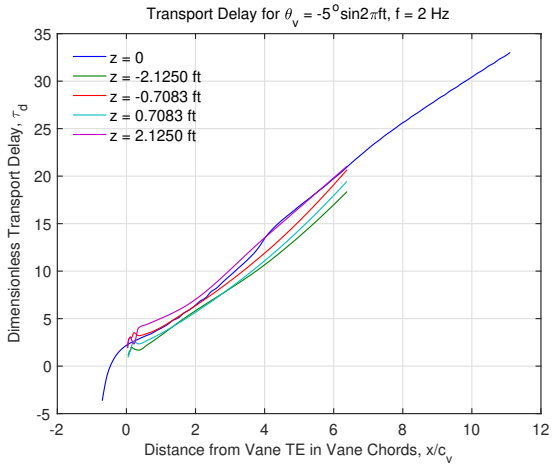

Figure 25. Gust Transport Delay for $5^\circ \sin 2\pi ft$, $f = 2$ Hz, $k_v = 0.0958$

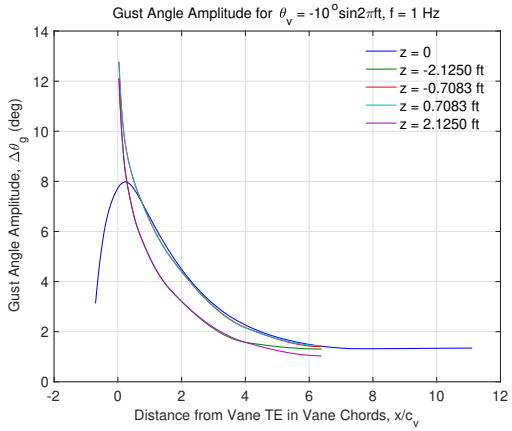

Figure 26. Gust Angle Amplitude for $10^\circ \sin 2\pi ft$, $f = 1$ Hz, $k_v = 0.0479$

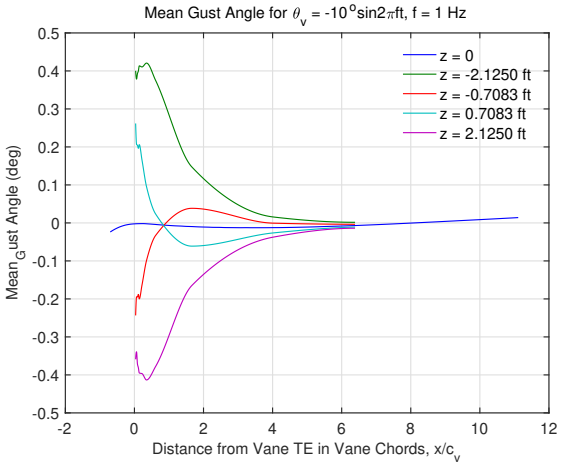

Figure 27. Mean Gust Angle for $10^\circ \sin 2\pi ft$, $f = 1$ Hz, $k_v = 0.0479$

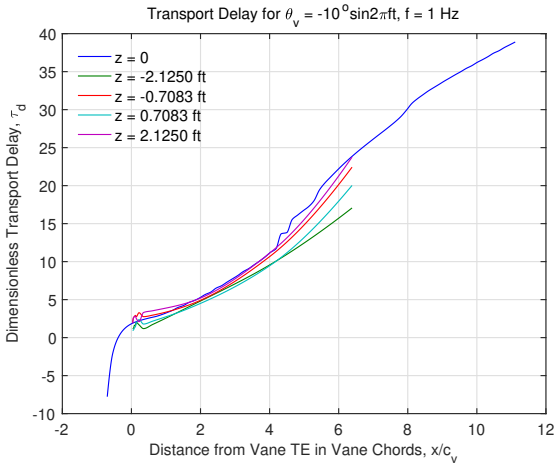

Figure 28. Gust Transport Delay for $10^\circ \sin 2\pi ft$, $f = 1$ Hz, $k_v = 0.0479$

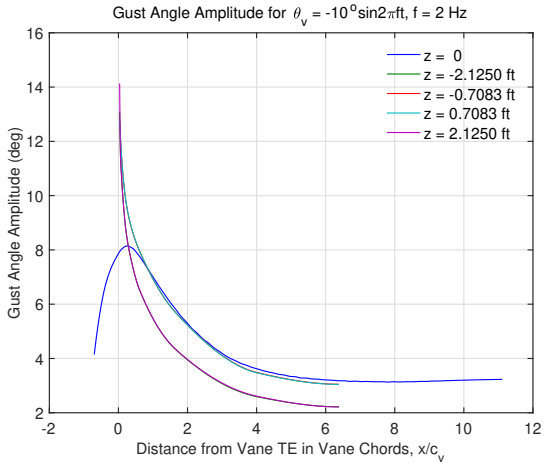

Figure 29. Gust Angle Amplitude for $10^\circ \sin 2\pi ft$, $f = 2$ Hz, $k_v = 0.0958$

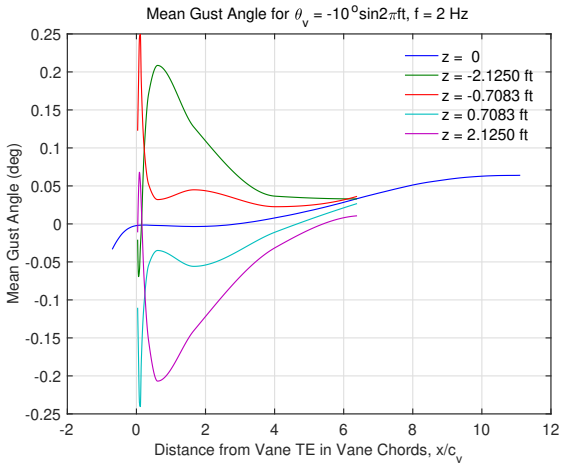

Figure 30. Mean Gust Angle for $10^\circ \sin 2\pi ft$, $f = 2$ Hz, $k_v = 0.0958$

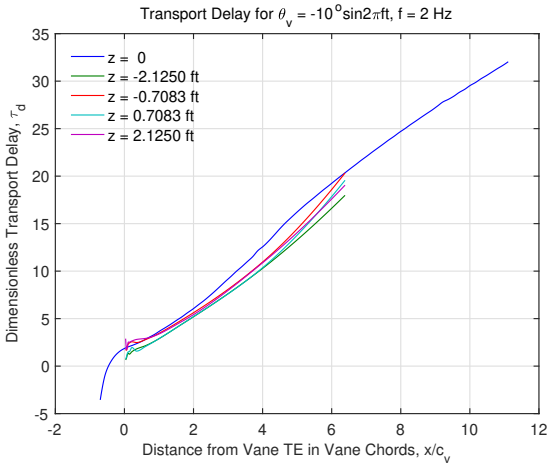

Figure 31. Gust Transport Delay for $10^\circ \sin 2\pi ft$, $f = 2$ Hz, $k_v = 0.0958$

Figures 32 and 33 show the ratio $r\,(x, 0)$ of the gust angle amplitude $\Delta\theta_g\,(x, 0)$ at the centerline to the gust generator vane pitch angle amplitude θ_0. It can be seen that the gust angle amplitude ratio is only a function of the gust generator vane angle amplitude. Increasing the gust vane angle amplitude is seen to cause a larger decrease in the steady-state gust angle amplitude ratio. The maximum gust angle amplitudes for both the gust generator vane amplitudes attain about the same value of about 0.8 at about the gust generator vane trailing edge. The dimensionless transport delay also shows a strong dependency on the gust generator vane amplitude. Below a distance of $4c_v$, the dimensionless transport delays for the two different gust generator angle amplitudes are in reasonably good agreement. The trend departs thereafter as the dimensionless transport delay for the 10° gust generator vane amplitude begins to increase to a larger value than that for the 5° gust generator vane amplitude. The behavior of the gust propagation is interesting and suggests a physical phenomenon. Further study may provide additional insight into this behavior.

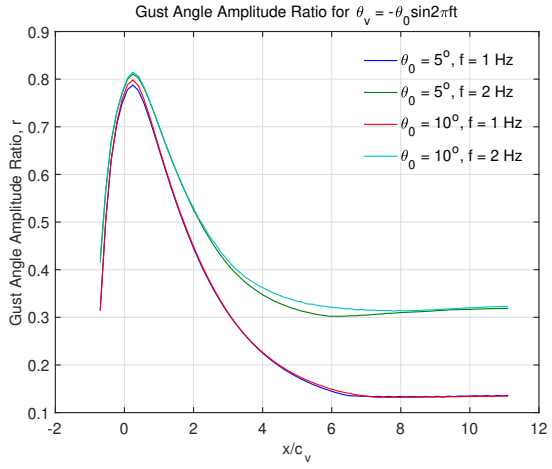

Figure 32. Gust Angle Amplitudes of Gust Generator

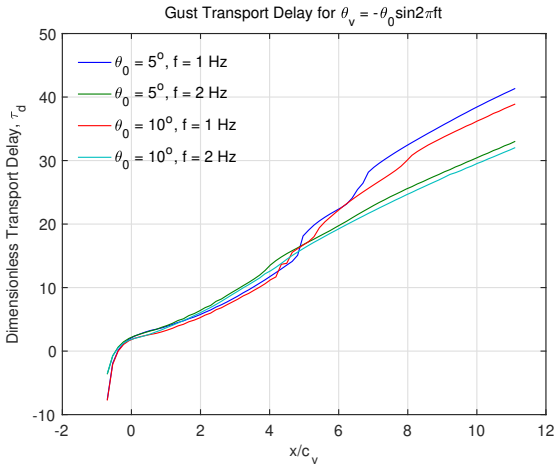

Figure 33. Gust Transport Delays of Gust Generator

V. Unsteady Lift Model

The gust propagation model is used to develop an unsteady lift model which will be used for developing an ASE model for the GLA control experiment. Using the gust propagation model, the unsteady lift of the wing can be estimated in a stripwise fashion. The estimation of the unsteady lift requires the knowledge of the three-dimensional (3D) wing aerodynamics. Such a model can be simulated by a wide variety of aerodynamic tools. On one end of the model fidelity spectrum, a 3D URANS CFD simulation for the whole entire system including the gust generator, the wing, and the test section could be done, but such an effort is hugely expensive. Moreover, it also involves a reduced-order modeling (ROM) to reduce the high-fidelity data to a simplified but relevant model for the purpose of the ASE modeling. At the other end of the spectrum, a pure vortex-lattice model of the wing alone could be developed. Then, using some analytical approaches for estimating the gust angle of attack, the unsteady lift of the wing could be estimated.

In our present approach, we adopt a varying-fidelity approach that brings together different techniques that are considered expedient to the task of estimating the unsteady lift for the primary purpose of developing an ASE model for the GLA control experiment. This approach utilizes 5 different modeling / experimental techniques of varying fidelity including:

- Unsteady two-dimensional (2D) RANS CFD simulations of the gust generator system in order to develop a gust propagation model as discussed in the previous sections
- A 2D interference aerodynamic model to estimate the aerodynamic interference between the gust generator vanes and the wing airfoil sections.
- A 3D wing aerodynamic model which could be a steady-state CFD model or potential flow model.
- Unsteady indicial response method for calculating unsteady lift of an airfoil in incompressible flow.
- Wind tunnel aerodynamic data such as lift curve slope.

A. Interference Aerodynamic Model of Gust Generator-Wing System

The present gust generator-wing system is a fully aerodynamically coupled system. The distance between the leading edge of the wing root section and the gust generator vane trailing edge is about $1c_v$. At the tip, the distance between the wing leading edge and the gust generator vanes is about $5.3c_v$. The gust generator vanes themselves are also coupled because they are technically in a cascade arrangement. The solidity is defined as the ratio of the airfoil chord to the spacing between the airfoils. The gust generator vanes have a solidity of 0.8824. In general, an airfoil in a cascade with a solidity less than about 0.2 is considered to be an isolated airfoil which can easily modeled by many standard aerodynamic tools. Garrick develops a thin

airfoil cascade aerodynamic theory and provides a simple method for estimating the lift curve slope which is a measure of the aerodynamic interference in a cascade of thin airfoils.[14] This formula is

$$c_{l_\alpha} = \varepsilon c^*_{l_\alpha} \tag{18}$$

$$\varepsilon = \frac{2}{\pi\sigma\sqrt{\cosh^2\gamma_0 - \sin^2\xi}} \tag{19}$$

$$\cos\xi \log\frac{\sqrt{\cosh^2\gamma_0 - \sin^2\xi} + \cos\xi}{\sinh\gamma_0} + \sin\xi\tan^{-1}\frac{\sin\xi}{\sqrt{\cosh^2\gamma_0 - \sin^2\xi}} - \frac{\pi\sigma}{2} = 0 \tag{20}$$

where ε is the cascade aerodynamic interference factor, $c^*_{l_\alpha} = 2\pi$ is the ideal 2D lift curve slope for an isolated airfoil, σ is the solidity, ξ is the stagger angle, and γ_0 is a parameter. The stagger angle ξ for the gust generator vanes is the gust generator vane pitch angle. The gust generator vanes are not exactly in a cascade because of the end walls, but it could be approximated as a cascade. Using this formula for $\xi = 0$ when the gust generator vanes are at a zero pitch angle, the lift curve slope for the gust generator vanes is about $0.6366c^*_{l_\alpha}$.

An analytical vortex model of the gust generator-wing system is developed using the image method to model the interference aerodynamics between the gust vanes and the wing. The image method is based on the aerodynamic conformal mapping which creates images of the gust vanes by reflecting the gust vanes about the two solid walls of the test section, as shown in Fig. 34. Thus, the total model includes four gust vanes on top and on the bottom mirrored about the two solid walls and the wing airfoil. Only two images of the two gust vanes next to the walls are shown in Fig. 34. A concentrated vortex is placed at the quarter chord of each airfoil. The induced velocities at the control point of the airfoil which is the three-quarter chord are then computed using the Bio-Savart law[25]

$$\Delta\mathbf{v} = \frac{\Gamma}{4\pi}\frac{d\mathbf{l}\times(\mathbf{r}_0 - \mathbf{r}_1)}{|\mathbf{r}_0 - \mathbf{r}_1|^3} \tag{21}$$

where Γ is the circulation, $d\mathbf{l}$ is the differential vortex filament, and $\mathbf{r}$ is a position vector.

The induced axial and vertical velocity components of the j-th airfoil on the i-th airfoil are computed by

$$u_{ij} = \frac{\Gamma_j}{c_{L_{\alpha_j}}}\frac{z_i - z_{0,j}}{(x_i - x_{0,j})^2 + (z_i - z_{0,j})^2} \tag{22}$$

$$w_{ij} = -\frac{\Gamma_j}{c_{L_{\alpha_j}}}\frac{x_i - x_{0,j}}{(x_i - x_{0,j})^2 + (z_i - z_{0,j})^2} \tag{23}$$

where (x_i, z_i) is the three-quarter chord coordinate of the i-th airfoil and $(x_{0,j}, z_{0,j})$ is the quarter-chord coordinate of the j-th airfoil.

The boundary condition of zero normal velocity on the i-th airfoil requires

$$\sum_{j=1}^{N} u_{ij}\sin\alpha_i + w_{ij}\cos\alpha_i + V_\infty(\alpha_i - \alpha_{0,i}) = 0 \tag{24}$$

for the gust generator vanes and wing airfoil, and

$$\sum_{j=1}^{N} u_{ij}\sin\alpha_i + w_{ij}\cos\alpha_i = 0 \tag{25}$$

for the image airfoils, where α_i is the angle of attack and $\alpha_{0,i}$ is the zero-lift angle of attack of the i-th airfoil.

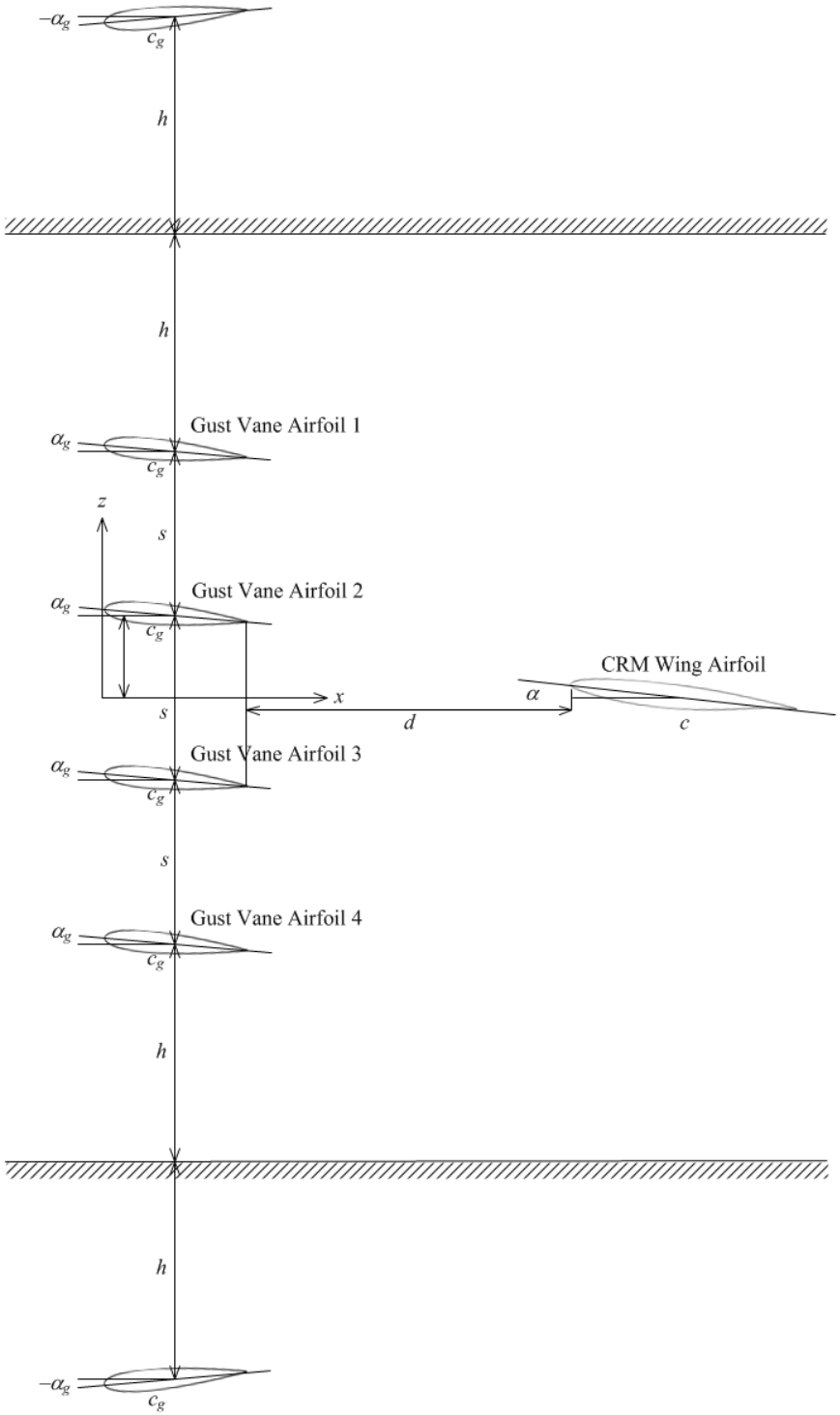

Figure 34. Vortex Model of Gust Generator-Wing System

Figure 35 shows the lift curves for the four gust generator vanes alone and with the three CRM wing airfoils at the tip, Yehudi break corresponding to the MAC, and root stations. The lift curves for the gust generator vanes alone are compared to the data computed by OpenFOAM. The two set of results show a similar trend. Gust generator vane 4 next to the floor has the highest positive lift and gust generator vane 1 next to the ceiling has the most negative lift. We note the nonlinear behavior in the lift curves. The average lift curve slope for the gust generator vanes is $c_{l_{\alpha,v}} = 5.0216$. This is to be compared to the ideal theoretical

cascade lift curve slope of $c_{l_\alpha} = 4.000$ from the Garrick's formula. The presence of the solid walls provides an additional lift increase. OpenFOAM gives a value of $c_{l_{\alpha,v}} = 5.2894$. We note that as the wing moves closer to the gust generator vanes the lifts on the gust generator vanes decrease, but the amount of lift reduction does not appear to be significant. However, the average lift curve slope for the gust generator vanes coupled to the wing root airfoil is estimated to be $c_{l_{\alpha,v}} = 4.1698$. This represents a 17% decrease in the lift curve slope. Figure 36 shows the lift curves for the CRM wing airfoils at the root, MAC, and tip coupled to the gust vanes at $c_l = 0$. As can be seen, the lift of the wing root is less than that of the wing tip due to the aerodynamic interference of the gust generator vanes. The lift reduction for the wing root airfoil is about 11%. Table 1 lists the lift curve slope values for different gust generator-wing configurations.

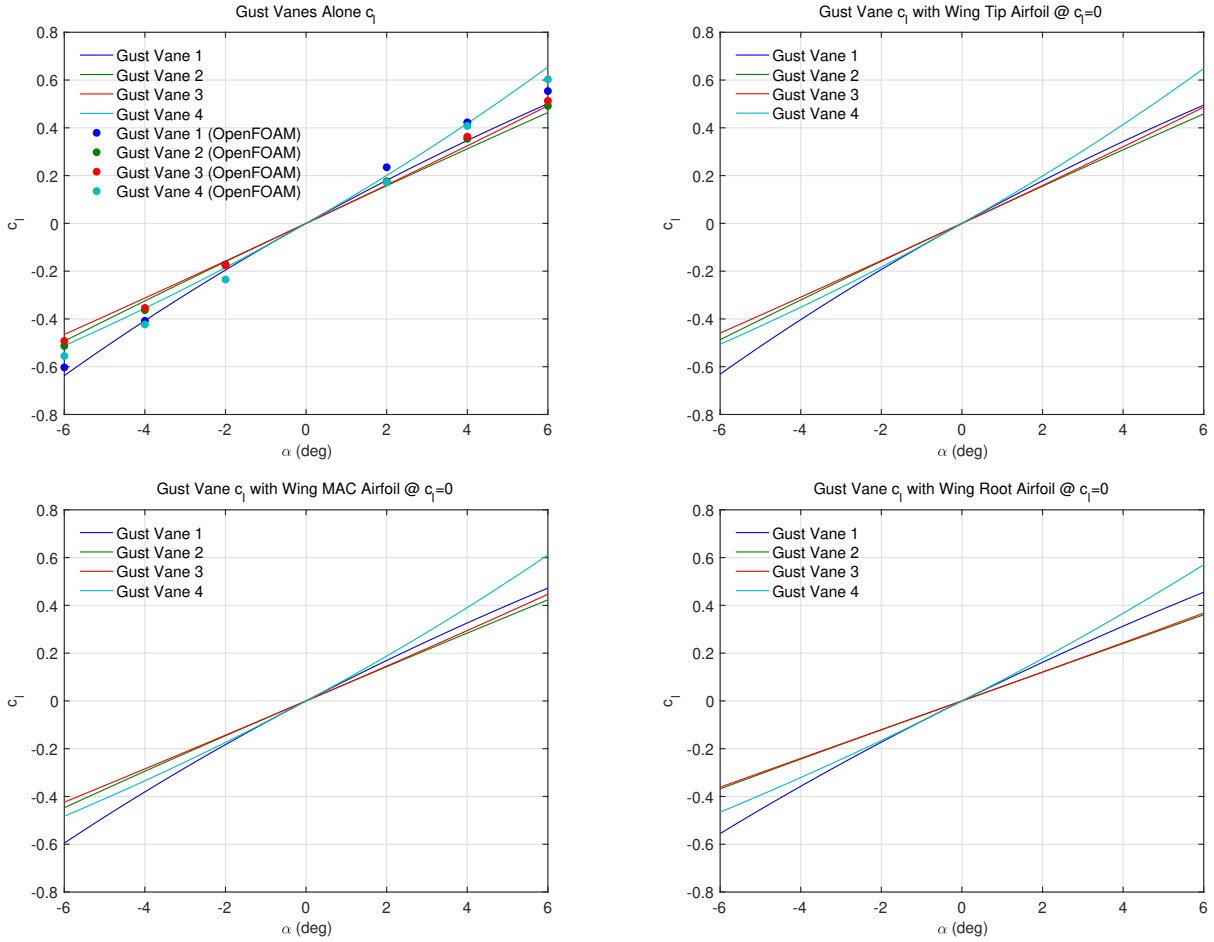

Figure 35. Interference Aerodynamic Model of Gust Generator-Wing System

c_{l_α}	Average Gust Vane	Wing Root	Wing MAC	Wing Tip
Gust Generator + Wing Root	4.1698	5.5913		
Gust Generator + Wing MAC	4.6427		5.9716	
Gust Generator + Wing Tip	4.9644			6.2364
Gust Generator Alone	5.0216	2π	2π	2π

Table 1. Lift Curve Slope c_{l_α} for Gust Generator-Wing Configurations

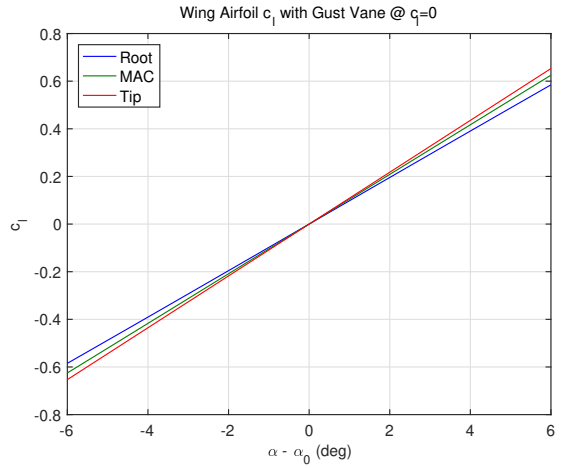

Figure 36. Lift Curves of Wing Airfoils + Gust Vanes @ $c_L = 0$

Figure 37 shows the variation of the ratios of the lift curve slopes to the theoretical lift curve slope value of 2π, denoted as ε, for the three CRM wing airfoils with the angle of attack of the gust generator vanes $\alpha_v = -\theta_v$. Thus , ε represents an aerodynamic interference factor due to the interactions of the gust generator vanes with the wing airfoils. This aerodynamic interference is the greatest when the gust generator vanes are at the most negative angle of attack and the wing airfoil is the closest to the gust generator vanes. Using the aerodynamic interference factor ε, the three-dimensional lift curve slope c_{L_α} can be corrected in a stripwise fashion.

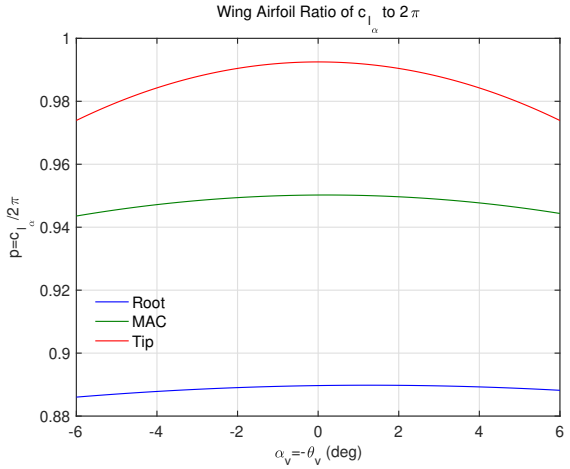

Figure 37. Variation of Lift Curve Slope Ratios of Wing Airfoils

B. Unsteady Lift Model

When the gust vertical velocity begins to strike the leading edge of the wing section, an unsteady lift is developed and can be computed by an indicial response model using the Duhamel's integral as

$$\bar{l}_g(x,t) = q_\infty c(x)\, c_{L_\alpha}(x,t) \left[\alpha_g(x,0,0)\,\psi(\tau) + \int_0^\tau \frac{d\alpha_g(x,0,\sigma)}{d\sigma}\psi(\tau-\sigma)\,d\sigma\right] \tag{26}$$

where $\tau = \frac{2U_\infty t}{c}$ is the distance in semi-chords traveled by the airfoil and $\psi(\tau)$ is the Küssner's function.[18]

In this formula, the wing section lift curve slope $c_{L_\alpha}(x,t)$ has been corrected for the interference aerodynamics of the gust generator-wing system as a function the of the gust generator angle of attack $\alpha_v(t)$. The gust angle of attack at the centerline for $z = 0$ is used in the formula. The dependency of the axial position

is implicitly accounted for by using a interpolation method. The unsteady lift can then be expressed as

$$\bar{l}_g(x,t) = q_\infty c(x)\, c_{L_\alpha}(x,t)\, r_g(x)\, r(x,0)\, \theta_v(t - t_d(x,0) - t_g(x)) \tag{27}$$

where $r_g(x)$ is the lift amplitude ratio and $t_g(x)$ is the additional transport delay due to the Küssner's function.

Dropping the function notations, the resulting unsteady lift due to gust can be expressed as

$$\bar{l}_g = q_\infty c c_{L_\alpha} r_g r \left[-\theta_v \cos\omega(t_d + t_g) + \frac{\dot{\theta}_v}{\omega} \sin\omega(t_d + t_g) \right] \tag{28}$$

For a sinusoidal gust with $\alpha_g = |\alpha_g| e^{i\omega t}$, the unsteady lift can also be evaluated as

$$\bar{l}_g = q_\infty c c_{L_\alpha} C_{sg}(k)\, \alpha_g \tag{29}$$

where

$$C_{sg}(k) = C(k)\left[J_0(k) - iJ_1(k)\right] + iJ_1(k) = F_{sg}(k) + iG_{sg}(k) \tag{30}$$

and J_0 and J_1 are the Bessel's functions.[15]

The unsteady lift then becomes

$$\begin{aligned} \bar{l}_g &= q_\infty c c_{L_\alpha} \left[F_{sg}(k)\, \alpha_g + \frac{\dot{\alpha}_g}{\omega} G_{sg}(k) \right] \\ &= q_\infty c c_{L_\alpha} r \left\{ -\theta_v \left[F_{sg}(k) \cos\omega t_d + G_{sg}(k) \sin\omega t_d \right] + \frac{\dot{\theta}_v}{\omega} \left[F_{sg}(k) \sin\omega t_d - G_{sg}(k) \cos\omega t_d \right] \right\} \end{aligned} \tag{31}$$

where $k = \frac{\omega c}{2U_\infty}$ is the reduced frequency of the wing section.

Equating the unsteady lift expressions in Eqs. (28) and (31) yields

$$r_g \cos\omega(t_d + t_g) = F_{sg}(k) \cos\omega t_d + G_{sg}(k) \sin\omega t_d \tag{32}$$

$$r_g \sin\omega(t_d + t_g) = F_{sg}(k) \sin\omega t_d - G_{sg}(k) \cos\omega t_d \tag{33}$$

from which r_g and t_g are obtained as

$$r_g(x) = \sqrt{F_{sg}^2(k) + G_{sg}^2(k)} \tag{34}$$

$$\tau_g(x) = \frac{1}{k_v} \tan^{-1} \frac{F_{sg}(k) \sin k_v \tau_d - G_{sg}(k) \cos k_v \tau_d}{F_{sg}(k) \cos k_v \tau_d + G_{sg}(k) \sin k_v \tau_d} - \tau_d \tag{35}$$

where $\tau_g = \frac{2U_\infty t_g}{c_v}$.

The unsteady lift generated by the gust generator acting on a swept wing with a wing sweep angle Λ is expressed as

$$l_g = \bar{l}_g \cos\Lambda = l_{\theta_v}\theta_v + l_{\dot{\theta}_v}\dot{\theta}_v \tag{36}$$

The integrated unsteady lift can then be computed as

$$L_g = L_{\theta_v}\theta_v + L_{\dot{\theta}_v}\dot{\theta}_v \tag{37}$$

where

$$L_{\theta_v} = \int_0^L l_{\theta_v} dx \tag{38}$$

$$L_{\dot{\theta}_v} = \int_0^L l_{\dot{\theta}_v} dx \tag{39}$$

Thus, the unsteady lift acting on the wing is a function of the gust generator pitch angle and pitch rate. For a flexible wing with active control surfaces, the total unsteady lift also includes the contributions of the wing elasticity and the control surfaces. Therefore, the total lift can be expressed in general as

$$L = \bar{L} + \bar{L}_x x + \bar{L}_u u + \bar{L}_w w \tag{40}$$

where $\bar{L}_w = \begin{bmatrix} L_{\theta_v} & L_{\dot{\theta}_v} \end{bmatrix}$, $w = \begin{bmatrix} \theta_v & \dot{\theta}_v \end{bmatrix}^\top$, x denotes the elastic states of the wing, u denotes the control surface deflections, $\bar{L}$ is the steady-state lift, and $\bar{L}_x$ and $\bar{L}_u$ are lift sensitivity vectors.

To assess how well the unsteady lift model is able to predict the total lift acting on the wing, the unsteady lift computed by the model is compared to the CFD simulations results. To that end, the wing section lift curve slope c_{L_α} must be computed from a 3D aerodynamic model coupled to a structural or finite-element model of the wing structure. The effect of wing aeroelasticity is such that the lift curve slope is reduced for a backward swept wing.[1] Instead of conducting an aero-structural modeling of the flexible CRM wing, we opt to use the lift curve slope C_{L_α} for the wing from an initial wind tunnel test entry in July 2019. Figure 38 shows a lift curve taken on one of the test runs during the test. The lift curve slope is computed to be 3.8572 in the linear region at about $C_L = 0.4$. This section lift curve slope is assumed to be constant and equal to this value. The test section dynamic pressure is 10 psf. Unsteady lift on the wing is measured by a side wall strain gauge balance while the gust generator is in a sinusoidal motion at a 2 Hz frequency and a 5° amplitude.

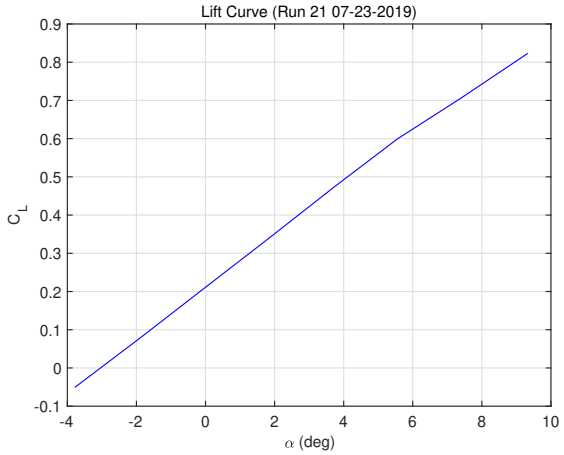

Figure 38. Lift Curve of CRM Wing (Run 21 on July 23, 2019)

The unsteady lift coefficients computed by the CFD simulations shown in Fig. 19 are used to compute the CFD-generated unsteady lift for comparison to the unsteady lift computed by the unsteady lift model. The simulations are conducted at an airspeed of 25 m/s corresponding to a dynamic pressure of 8 psf. The ideal lift curve slope of the wing airfoil is assumed to be about 2π. A correction factor of 0.7674 ($\frac{10}{8}\frac{3.8572}{2\pi}$) is applied to the CFD-computed lift values.

Figures 41 - 39 show the unsteady lift at the three CRM wing stations for a gust vane sinusoidal input at 2 Hz frequency and 5° amplitude for a dynamic pressure of 10 psf. The unsteady lift model produces excellent agreement with the CFD result at the wing MAC station, but has less agreement at the wing root and tip station. The discrepancy in the unsteady lift at the wing tip only amounts to 0.5 lb/ft but is larger at the wing root.

Figure 42 shows the total integrated unsteady lift computed from the unsteady lift model. The unsteady lift amplitude is 11.08 lbs. Experimental data for unsteady lift are available from the wind tunnel test. Figure 43 is the plot of the lift force measurement from the side wall balance with a sinusoidal motion of the gust generator at a 2 Hz frequency and 5° amplitude from one of the test runs in August 2019. The measured unsteady lift is 13.26 lbs using the last period in the data. This unsteady lift also includes the wing dynamic response, so a direct comparison is not possible. A dynamic response analysis is performed[16] for the CRM wing to compute the unsteady lift response due to the elastic state contribution which is plotted in Fig. 44. For the open-loop response without active controls, the computed unsteady lift response is 13.54 lbs using the last period when the response settles to a steady-state sinusoidal motion. This indicates that the unsteady lift model results in excellent agreement with the measured unsteady lift response.

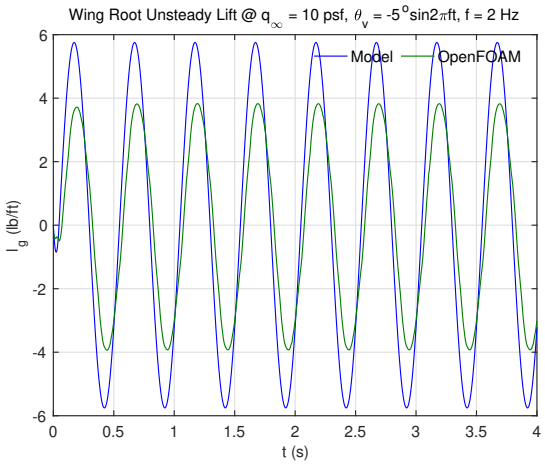

Figure 39. Unsteady Lift at CRM Wing Root for $5^\circ \sin(2\pi f t)$, $f = 2$ Hz

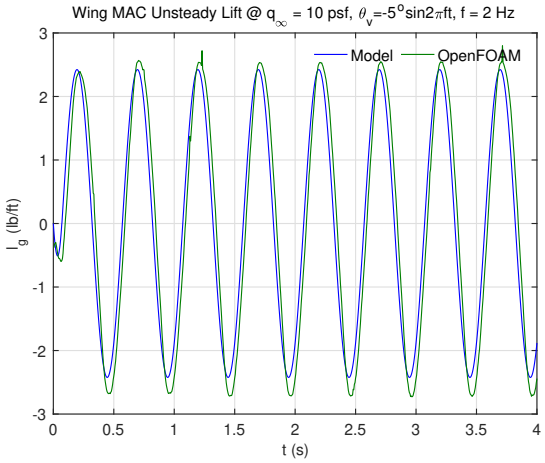

Figure 40. Unsteady Lift at CRM Wing MAC for $5^\circ \sin(2\pi f t)$, $f = 2$ Hz

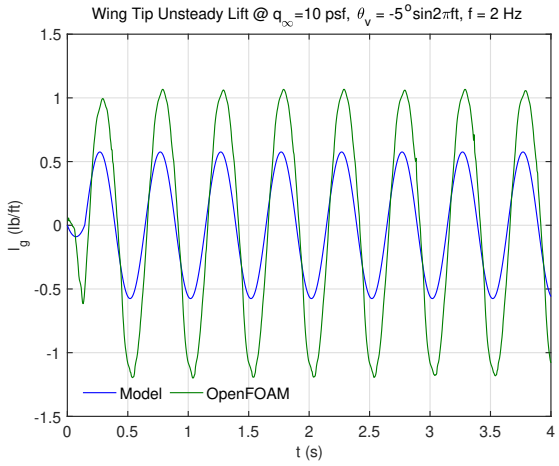

Figure 41. Computed Unsteady Lift at CRM Wing Tip for $5^\circ \sin(2\pi f t)$, $f = 2$ Hz

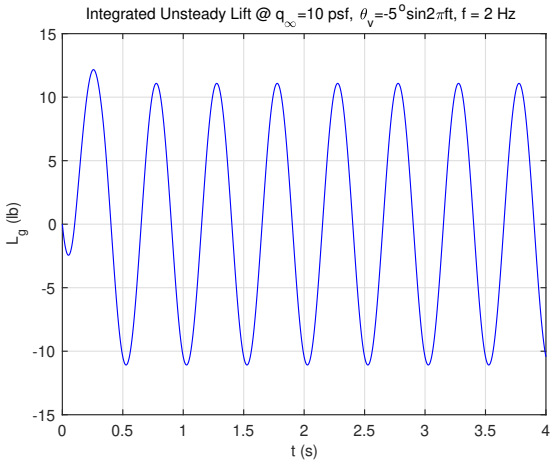

Figure 42. Total Integrated Unsteady Lift for $5^\circ \sin(2\pi f t)$, $f = 2$ Hz

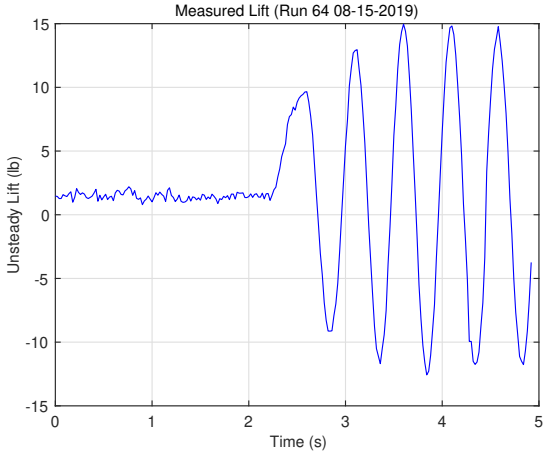

Figure 43. Measured Unsteady Lift Response

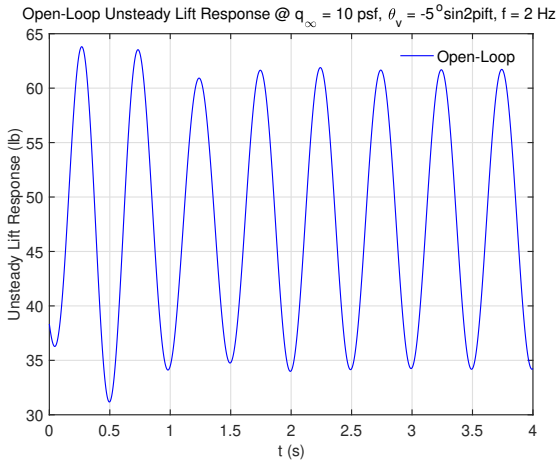

Figure 44. Measured Unsteady Lift Response

The transport delay of the unsteady lift response can be inferred from Fig. 45 which shows the measured

zero-mean unsteady lift in relation to the gust generator vane pitch angle. When the gust generator vanes are in a negative pitch angle, a positive lift is generated. A transport delay of 0.12 sec is estimated between the unsteady lift response and the gust generator vane pitch angle. The integrated lift in Fig. 42 computed by the unsteady lift model shows a 0.13 sec transport delay compared to a 0.14 sec transport delay estimated from Fig. 44 for the open-loop unsteady lift response. Thus, in summary, the unsteady lift model accurately captures both the amplitude and the transport delay of the gust propagation generated by the gust generator.

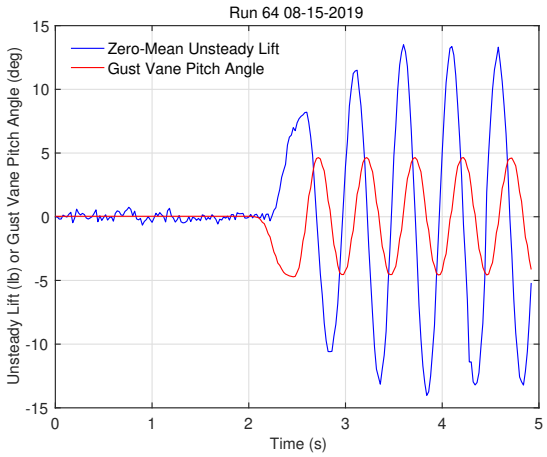

Figure 45. Measured Unsteady Lift Response in Relation to Gust Generator Vane Pitch Angle

VI. Conclusions

A computational investigation of induced flow by a four -vane gust generator is performed using the URANS approach with the k-ω SST turbulence model. The decay of the induced vertical velocity and the transport lag response are observed and analyzed. A gust propagation model is developed to analyze the the characteristics of the gust amplitude and transport delay as a function of the frequency and amplitude of the gust generator vane sinusoidal motion. The model reveals a stronger dependency of the gust propagation characteristics on the gust generator vane motion amplitude than frequency. An unsteady lift model is developed using a varying-fidelity approach of combining the URANS-generated gust propagation model with an interference aerodynamic model of the combined gust generator-wing system and an indicial response model for computing the unsteady lift response in a sinusoidal gust field. The computed integrated unsteady lift demonstrates an excellent agreement in both the amplitude and transport delay when comparing the measured unsteady lift response from the wind tunnel data to the computed open-loop response of the unsteady lift.

Acknowledgment

The authors wish to acknowledge NASA Advanced Air Transport Technology project for the funding support of this work. The authors also acknowledge University of Washington personnel who support the project. The gust load alleviation experiment is conducted with the funding support by NASA SBIR program under the NASA SBIR Phase II-X Contract NNX15CA16C and Phase III Contract 80NSSC17C0063.

References

[1]Nguyen, N., Precup, N., Urnes, J., Nelson, C., Lebofsky, S., Ting, E., and Livne, E., "Experimental Investigation of a Flexible Wing with a Variable Camber Continuous Trailing Edge Flap Design," 32nd AIAA Applied Aerodynamics, AIAA 2014-2441, June 2014.

[2]Nguyen, N., "Elastically Shaped Future Air Vehicle Concept," NASA Innovation Fund Award 2010 Report, October 2010, Submitted to NASA Innovative Partnerships Program, http://ntrs.nasa.gov/archive/nasa /casi.ntrs.nasa.gov/20110023698.pdf

[3]Nguyen, N. and Urnes, J., "Aeroelastic Modeling of Elastically Shaped Aircraft Concept via Wing Shaping Control for

Drag Reduction," AIAA Atmospheric Flight Mechanics Conference, AIAA-2012-4642, August 2012.

[4]Nguyen, N., Trinh, K., Reynolds, K., Kless, J., Aftosmis, M., Urnes, J., and Ippolito, C., "Elastically Shaped Wing Optimization and Aircraft Concept for Improved Cruise Efficiency," 51st AIAA Aerospace Sciences Meeting, AIAA-2013-0141, January 2013.

[5]Hashemi, K., Nguyen, N., Drew, M., Ting, E., and Chaparro, D., "Performance Optimizing Gust Load Alleviation Control of Flexible Wing Aircraft," AIAA Guidance, Navigation, and Control Conference, AIAA-2018-0623, January 2018.

[6]Fonte, F. et al, "Design, Manufacturing and Validation of a Gust Generator for Wind Tunnel Test of A Large Scale Aeroelastic Model," ICAS-2016

[7]Lancelot, Paul M.G.J., Sodja, J., Werter, N. P.M., and Breuker R. D., "Design and testing of a low subsonic wind tunnel gust generator", Advances in Aircraft and Spacecraft Science, Vol. 4, No. 2 (2017) 125-144

[8]Ham, N.D., Bauer, P.H., and Lawrence, T.L., "Wind Tunnel Generation of Sinusoidal Lateral and Longitudinal Gusts by Circulation Control of Twin Parallel Airfoils", NASA CR 137547, August 1974.

[9]Redd, T.L., Hanson, P.W., and Wynne, E.C., "Evaluation of a Wind Tunnel Gust Response Technique Including Correlations with Analytical and Flight Test Results", NASA Technical Paper 1501, November 1979.

[10]Tang, D.M., Cizmas, P.G.A., and Dowell, E.H., "Experiments and Analysis for a Gust Generator in a Wind Tunnel", Journal of Aircraft, Vol. 33, No. 1, January-February 1996, pp. 139-148

[11]Cizmas, P.G.A., Tang, D., and Dowell, E.H., "Flow about a Slotted Cylinder-Airfoil Combination in a Wind Tunnel", Journal of Aircraft, Vol. 33, No. 4, July-August 1996, pp. 716-721

[12]Xu, H., Xing, S., and Ye, Z., "Numerical Study of an Airfoil/Rotating-Slotted-Cylinder Based Flutter Exciter", Journal of Aircraft, Vol. 52, No. 6., November-December 2015, pp. 2100-2105

[13]Tang, D., and Dowell, E.H., "Experimental and Theoretical Study of Gust Response for High-Aspect-Ratio Wing", AIAA Journal, 2002, Vol. 40, No. 3, pp. 419-429

[12]Tang, D., Henry, J.K., and Dowell, E.H., "Nonlinear Aeroelastic Response of Delta Wing to Periodic Gust". Journal of Aircraft, 2000, Vol. 37, No. 1, pp. 155-164

[13]Charles Poussot-Vassal, Fabrice Demourant, Arnaud Lepage, Dominique Le Bihan. 2017. "Gust Load Alleviation: Identification, Control, and Wind Tunnel Testing of a 2-D Aeroelastic Airfoil," IEEE Transactions on Control Systems Technology 25:5, 1736-1749

[14]Babbar, Y., Suryakumar, V.S., and Strganac, T.W., "Experiments in Aeroelastic Response and Control Under Gust", AIAA Paper 2013-1637

[15]Babbar, Y., Suryakumar, V.S., Strganac, T.W., Mangalam, A. S., "Measurement and Modeling of Aeroelastic Response under Gust", AIAA, 2015-2724

[16]Harding,S.F., and Bryden, I.G., "Generating controllable velocity fluctuations using twin oscillating hydrofoils. Journal of Fluid Mechanics", 2012, 713, 150-158

[17]Harding, S.F., Payne, G.S., and Bryden, I.G., "Generating controllable velocity fluctuations using twin oscillating hydrofoils: experimental validation", Journal of Fluid Mechanics, July 2014, pp. 113-123

[18]Neumann, J., Mai, H., "Gust response: Simulation of an aeroelastic experiment by a fluid–structure interaction method", Journal of Fluids and Structures, 2013, 38, pp. 290-302.

[19]Wildschek, A., Maier, R., Hoffmann, F., Steigenberger, J., Laulfuss, K.-H., Breitsamter, C., Allen, A., Adams, N., Baier, H., Giannopoulos, T., and Dafnis, A., "Wind Tunnel Testing of an Adaptive Control System for Vibration Suppression on Aircraft", AIAA, 2007-6331

[20]Mai, H., Neuman, J., Hennings, H., "Gust Response: A Validation Experiment and Preliminary Numerical Simulations", International Forum on Aeroelasticity and Structural Dynamics, 2011, Paper IFASD 2011-051.

[21]Neumann J., Mai H., "Gust response: Simulation of an aeroelastic experiment by a fluid–structure interaction method", Journal of Fluids and Structures, 2013, 38, pp. 290–302

[22]Ricci S., Scotti A., "Wind Tunnel Testing of an Active Controlled Wing under Gust Excitation", AIAA, 2008-1727

[23]Saddington A.J., Finnis M.V., Knowles K., The characterisation of a gust generator for aerodynamic testing, Proc IMechE Part G: J Aerospace Engineering, 229(7):1214-1225, June 2015

[24]Bateman, Daniel Gretz, "Design and Qualication of an Upstream Gust Generator in a Low-Speed Wind Tunnel" (2017). Aerospace Engineering Sciences Graduate Theses & Dissertations. 196

[25]Wood, K.T., Cheung, R.M., Richardson, T., and Cooper, J., "A New Gust Generator for Low Speed Wind Tunnel: Design and Commissioning", AIAA, 2017-0502

[26]Quenzer, J., Zongolowicz, A., Hinson, K.A., Barzgaran, B., Livne, E., Mesbahi, M., and Morgansen, K., "Model for Aeroelastic Response to Gust Excitation", Paper AIAA, 2019-2031

[27]OpenFOAM User Guide, Version 4, 2016 28. Menter, F., "Two-Equation Eddy-Viscosity Turbulence Models for Engineering Applications," AIAA Journal, Vol. 32, No. 8, 1994, pp. 1598–1605.

[28]Menter, F., "Two-Equation Eddy-Viscosity Turbulence Models for Engineering Applications," AIAA Journal, Vol. 32, No. 8, 1994, pp. 1598–1605.

[14]Garrick, I. E., "On the Plane Potential Flow Past a Lattice of Arbitrary Airfoil," NACA Report No. 788, 1944.

[25]Anderson, J., *Fundamentals of Aerodynamics*, McGraw-Hill, New York, 2001.

[15]Bisplinghoff, R. L., Ashley, H., and Halfman, R. L., *Aeroelasticity*, Dover Publications, Inc., New York, 1996.

[16]Nguyen, N., Cramer, N., Hashemi, K., Drew, M., Xiong, J., Mundt, T., Mor, M., Livne, E., Jackson, J., Wise, R., Shultz, A., Boskovic, J., "Progress on Gust Load Alleviation Wind Tunnel Experiment and Aeroservoelastic Model Validation for a Flexible Wing with Variable Camber Continuous Trailing Edge Flap System," AIAA Structural Dynamics Conference, January 2020.